Electronic supplementary information

High-coordination Fe-N$_4$SP single-atom catalysts via the multi-shell synergistic effect for enhanced oxygen reduction reaction of rechargeable Zn-air battery cathodes

Jiaqi Liu [a†], Weibin Chen [b†], Shuang Yuan [a,d,e*], Tie Liu [c], Qiang Wang [a,c*]

a School of Metallurgy, Northeastern University, Shenyang 110819, China.

b School of Materials Science and Engineering, Peking University, Beijing 100871, China.

c Key Laboratory of Electromagnetic Processing of Materials (Ministry of Education), Northeastern University, Shenyang 110819, China.

d Key Laboratory of Ecological Metallurgy of Multimetallic Mineral (Ministry of Education), Northeastern University, Shenyang 110819, China.

e Engineering Research Center of Frontier Technologies for Low-carbon Steelmaking (Ministry of Education), Liaoning Low-carbon Steelmaking Technology Engineering Research Center, Shenyang 110819, China

† These authors contributed equally to this work.

*Corresponding author. Email: yuans@smm.neu.edu.cn; wangq@mail.neu.edu.cn; Tel.: +86-24-83681171.

Contents

S1 Experimental Details

S1.1 Materials

Zinc nitrate hexahydrate ($Zn(NO_3)_2 \cdot 6H_2O$, 99%) is purchased from Tianjin Yongda Chemical Reagent Co., Ltd. Iron phthalocyanine (FePc, 98%), 4, 4'-oxydiphenol (97%), trichloromelamine (95%) and potassium hydroxide (KOH, 95%) are purchased from Shanghai Macklin Biochemical Technology Co., Ltd. 2-methylimidazole (98%), 4, 4′-sulfonyldiphenol (99%) and phosphonitrilic chloride trimer (98%) are purchased from Shanghai Aladdin Biochemical Technology Co., Ltd. Triethylamine is purchased from Tianjin Hengxing Chemical Preparation Co., Ltd. Ethanol and methanol are purchased from Tianjin Fuyu Fine Chemical Co., Ltd. Commercial Pt/C (20 wt% platinum in carbon) and RuO_2 catalysts are purchased from Shanghai Hesen Electric Co., Ltd. and Strem Chemicals, Inc., respectively. All chemicals are used without further purification. All aqueous solutions were prepared with high-purity de-ionized water.

S1.2 Material preparation

Preparation of ZIF-8/FePc: ZIF-8/FePc is synthesized by adding iron phthalocyanine (FePc) into the typical preparation method of ZIF-8. In this way, 5.95 g (20 mmol) of $Zn(NO_3)_2 \cdot 6H_2O$, as well as 2-methylimidazole (6.568 g, 80 mmol) and FePc (50, 100, 150, 200 mg), were respectively dissolved in 80 mL methanol and sonicated until uniformly dispersed. Subsequently, The solution containing $Zn(NO_3)_2$ was rapidly poured into 2-methylimidazole solution under magnetic stirring and stirred continuously for 24 h at room temperature. The product was obtained by centrifugation and washed with methanol, then dried in a vacuum overnight to obtain ZIF-8/FePc.

Preparation of ZIF-8/FePc@PZS: 100 mg of ZIF-8/FePc was ultrasonically dispersed in 40 mL methanol and labeled as solution A. 20 mL of a methanol solution containing phosphonitrilic chloride trimer (150 mg) and 4, 4′-sulfonyldiphenol (335 mg) was added dropwise to solution A using the partition funnel and stirred for 5 min, then 1 mL of triethylamine was added to the above-mixed solution. The reaction was carried out continuously at room temperature for 6 h, then ZIF-8/FePc@PZS was collected by centrifugation and dried in a vacuum. In contrast, ZIF-8/Fe@PZM was

prepared with a similar process of ZIF-8/FePc@PZS, except that 4, 4′-sulfonyldiphenol (335 mg) was replaced by 4, 4'-oxydiphenol (270 mg), while ZIF-8/FePc@MZS was prepared though replacing phosphonitrilic chloride trimer (150 mg) by trichloromelamine (198 mg). The ZIF-8@PZS was prepared with the same synthesis procedure dy using ZIF-8 instead of ZIF-8/FePc.

Preparation of Fe-N$_4$SP/NPS-HC: Fe-N$_4$SP/NPS-HC was prepared by high-temperature pyrolysis and acid etching of ZIF-8/FePc@PZS. Specifically, ZIF-8/FePc@PZS was placed in a tube furnace and maintained for 2 h at 950°C with a heating rate of 5 °C/min under an Ar/NH$_3$ atmosphere. Then, the collected product was continuously stirred in 1 M HCl at 40°C for 12 h and obtained Fe-N$_4$SP/NPS-HC.

Preparation of a series of reference samples: The Fe-N$_4$S/NS-HC and Fe-N$_4$P/NPC were synthesized by pyrolysis of ZIF-8/FePc@MZS and ZIF-8/FePc@PZM with the same conditions as Fe-N$_4$SP/NPS-HC. The Fe-N$_4$/NC and NPS-HC were obtained by direct pyrolysis of ZIF-8/FePc and ZIF-8@PZS at 950°C under an Ar/NH$_3$. While Fe-N$_4$/NPSC was prepared by secondary calcination of Fe-N$_4$/NC@PZS under the same pyrolysis process. Then, the samples with different FePc contents were labeled as Fe-N$_4$SP/NPS-HC-0.5, Fe-N$_4$SP/NPS-HC, Fe-N$_4$SP/NPS-HC-1.5, and Fe-N$_4$SP/NPS-HC-2. Fe-N$_4$SP/NS-HC-Ar was obtained by pyrolysis of ZIF-8/FePc@PZS under an Ar atmosphere instead of Ar/NH$_3$.

The flow chart of synthesis procedure including the target sample and references was shown in Schematic S1.
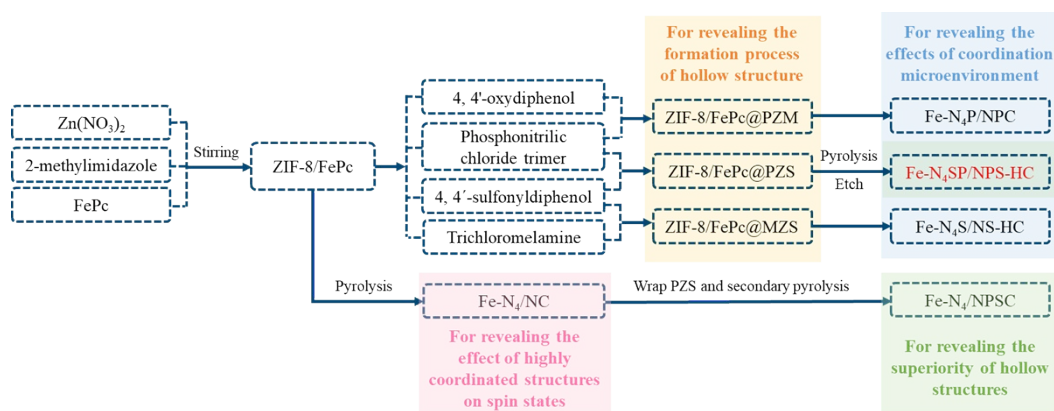
Schematic S1 The synthesis procedure and preparation purpose of the target sample and references.

S1.3 Material characterizations

The microstructures of the as-prepared materials were characterized by scanning electron microscopy (SEM, ZSISS GeminiSEM 300) at 3 kV, transmission electron microscopy (TEM, FEI Tecnai G2 F20) at 200 kV, and aberration-corrected HADDF-STEM (FEI Themis Z) at 200 kV. X-ray diffraction (XRD) patterns were conducted with a Rigaku Ultima IV diffractometer. Fourier transform infrared (FT-IR) spectrum was performed on a Bruker ALPHA spectrometer using KBr pellets. X-ray photoelectron spectroscopy (XPS) was conducted using a Thermo Scientific K-Alpha instrument with Al Kα radiation to analyze the chemical composition. Thermogravimetric analysis (TG) was performed on a Rigaku TG/DTA8122 between 30°C and 1000°C at a heating rate of 10 °C/min in the Ar atmosphere. Renishaw 2000 model confocal microscopy Raman spectrometer. The specific surface area was calculated by analyzing the N_2 adsorption/desorption isotherms (Quantachrome Nova 4000e) of Brunauer-Emmett-Teller (BET). The contents of iron elements were tested by an inductively coupled plasma optical emission Spectrometer (ICP-OES, Agilent 5110). Electron paramagnetic resonance (EPR) measurements were conducted with Bruker EMXnano. The zero-field cooling (ZFC) temperature-dependent magnetic susceptibility was measured by superconducting quantum interference devices (Quantum Design PPMS-9) with a temperature range from 3 to 300 K under the magnetic field of 1000 Oe.

XAFS measurements and data analysis details. The X-ray absorption spectra (XAS) of Fe K-edge were performed with Si(111) crystal monochromators at the BL14W1 Beamline at the Shanghai Synchrotron Radiation Facility (SSRF) (Shanghai, China). Before the analysis at the beamline, samples were placed into aluminum sample holders and sealed using Kapton tape film. The XAFS spectra were recorded at room temperature using a 4-channel Silicon Drift Detector (SDD) Bruker 5040. Fe K-edge extended X-ray absorption fine structure (EXAFS) spectra were recorded in transmission/fluorescence mode. Negligible changes in the line-shape and peak position of Fe K-edge XANES spectra were observed between two scans taken for a specific sample. Fe foil, FePc, FeS_2, and Fe_2O_3 were used as references and measured

in a transmission mode using an ionization chamber.

The spectra were processed and analyzed in Athena for background, pre-edge line, and post-edge line calibrations. Then Fourier transformed fitting was carried out in Artemis. The k_3-weighted EXAFS spectra were obtained by subtracting the post-edge background from the overall absorption and then normalizing with respect to the edge-jump step. The coordination number (CN), bond length, Debye-Waller factor (R), and E_0 shift (ΔE_0) were fitted without anyone being fixed, the σ^2 was set. To obtain the quantitative structural parameters around central atoms, least-squares curve parameter fitting was performed using the ARTEMIS module. For Wavelet Transform analysis, the $\chi(k)$ exported from Athena was imported into the Hama Fortran code.

S1.4 Electrochemical measurements

All the electrochemical measurements were carried out with an electrochemical workstation (VSP, Bio-Logic) in a three-electrode system. The as-prepared catalysts and Pt/C were made into traditional catalyst ink for the preparation of working electrode. In this way, 5 mg of sample powder was dispersed in 1 mL of ethanol and 50 µL of Nafion solution by sonicating for 1 h to obtain a homogeneous catalyst ink. Then 20 µL of the dispersion was drop-cast onto the glassy carbon (GC) electrode surface and air-dried. The mass loading was about 0.5 mg cm^{-2}. The electrochemical measurements were conducted in 0.1 M KOH and 0.1 M HClO$_4$ electrolytes. The Hg/HgO (1 M KOH) electrode and Ag/AgCl (saturated KCl) were used as the reference electrode in alkaline and acidic media, respectively. While the graphite rod was used as the counter electrode.

The cyclic voltammogram (CV) tests were acquired in an N$_2$- or O$_2$-saturated solution with a scan rate of 10 mV s^{-1}. Linear sweep voltammetry curves (LSV) were recorded at different speeds of 1600 rpm in an O$_2$-saturated solution with a scan rate of 5 mV s^{-1} without being *iR*-corrected. Before all the electrochemical characterizations, the continuous sweep of the corresponding voltage range was measured until the steady CV curve was obtained. The recorded potential values vs. Hg/HgO and Ag/AgCl were converted to a reversible hydrogen electrode (RHE) scale according to the Nernst equation ($E_{RHE} = E_{ref} + 0.059 \times pH + 0.098/0.198$). The double-layer capacitance (C_{dl})

was measured through CV curves at the non-Faradaic potential with different scan rates (10 mV s^{-1} to 60 mV s^{-1}) to evaluate the electrochemical surface area (ECSA).

According to the LSV curves at the different potentials, the electron transfer number (n) was calculated according to the Koutecky-Levich (K-L) equations:

$$\frac{1}{J} = \frac{1}{J_L} + \frac{1}{J_k} = \frac{1}{B\omega^{1/2}} + \frac{1}{n\mathrm{F}kC_O}$$

(1)

$$B = 0.62n\mathrm{F}C_O D_O^{2/3} v^{-1/6}$$

(2)

Where J is the measured current density using a rotating disk electrode (RDE), while J_L and J_k are the diffusion-limiting and kinetic current density, respectively. ω reflects the disk angular velocity, k is the electron transfer rate constant, n is the electron transfer number of per oxygen molecule, F is the Faraday constant (96485 C mol^{-1}). In addition, C_O is the saturated O$_2$ concentration (1.2×10^{-3} mol cm^{-3} for 0.1 M KOH and 1.26×10^{-3} mol cm^{-3} for 0.1 M HClO$_4$), while the D_O is the O$_2$ diffusion coefficient (1.9×10^{-5} cm^2 s^{-1} for 0.1 M KOH and 1.93×10^{-5} cm^2 s^{-1} for 0.1 M HClO$_4$). Besides, v is the kinetic viscosity of solution (0.01 cm^2 s^{-1}).

Moreover, the number of electrons transferred and yield of hydrogen peroxide were obtained through rotating ring-disc electrode (RRDE) and calculated with the following equations, respectively:

$$n = 4 \times \frac{J_D}{J_D + J_R/N}$$

(3)

$$H_2O_2\% = \frac{J_R/N}{J_D + J_R/N} \times 200\%$$

(4)

Where J_D and J_R are the disk and ring current densities, respectively. N is the ring collection efficiency and is determined to be 0.37.

The long-term durability was evaluated in two ways, one was to conduct a continuous CV scan between 0.6 and 1.0 V (vs. RHE) in O$_2$-saturated 0.1 M KOH or 0.1 M HClO$_4$ and record the LSV curves of initial and 10k cycles. And another was to use chronoamperometric (i-t) measurement in the corresponding solution at a rotation rate of 1600 rpm. To test the tolerance to CH$_3$OH, chronoamperometric measurements is

carried out in an O_2-saturated mixed solution, in which 5% of CH_3OH was injected into 0.1 M KOH or 0.1 M $HClO_4$.

S1.5 Zn-air battery assembly and measurements

The home-made rechargeable Zn-air battery (ZAB) was assembled by carbon paper loading the catalysts as air cathode, the polished zinc plate as anode, and 6 M KOH containing 0.2 M zinc acetate as electrolyte. Among them, the catalyst is composed of a mixed ink of Fe-N$_4$SP/NPS-HC, Fe-N$_4$P/NPC, and Pt/C mixed with RuO_2 (1:1), as well as the mass loading was about 0.5 mg cm^{-2}.
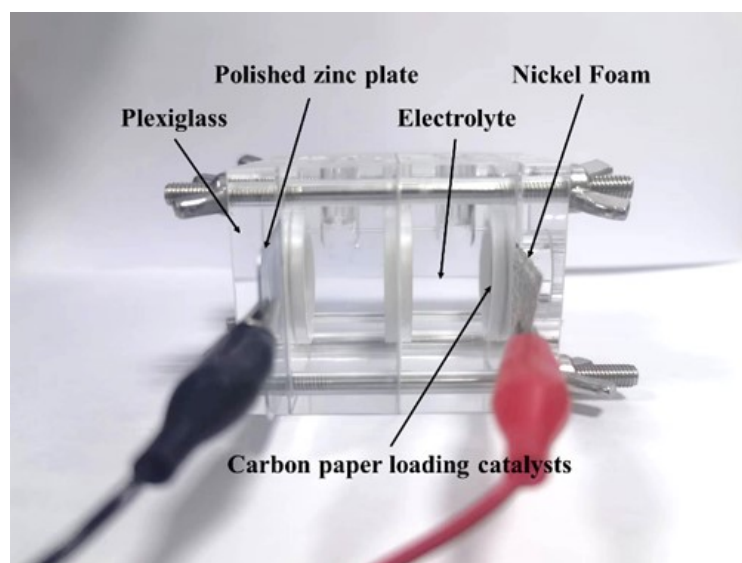
Schematic S2 The detailed cell configuration of home-made rechargeable Zn-air battery.

The electrochemical tests of ZAB were conducted on an electrochemical workstation (VSP, Bio-Logic) in a two-electrode system and a Land battery measurement system (Land, China) under ambient air. The galvanodynamic charge/discharge curves were recorded by linear sweep voltammetry (5 mV s^{-1}, at room temperature). The rate performance is evaluated by the multi-step chronopotentiometry curve at different current densities. And the cycling curves were obtained through 400 s for a cycle.

S2 Computational Details

S2.1 Calculation of unpaired d electrons for Fe ions

The effective magnetic moment (μ_{eff}) of Fe-N$_4$SP/NPS-HC and Fe-N$_4$/NC was evaluated based on the Langevin theory: $\mu_{eff} = \sqrt{8C}\mu_B$. Here, C is the Curie constant and obtained by fitting the curve of χ^{-1}-T according to the Curie-Weiss law $\chi = C/(T-\Theta)$, in which the slope of the curve of χ^{-1}-T is 1/C, while T means absolute temperature (K),

as well as χ and Θ are the susceptibility and Curie-Weiss temperature, respectively. The χ is derived from the magnetization (M) following the equation of χ=M/H, where H is the magnetic field intensity (i.e. 1000 Oe in this work).

S2.2 DFT calculations

We conducted spin-polarized density functional theory simulations using the Vienna ab initio simulation package (VASP6.1.0).[1] We employed the PAW potentials to describe the electron-ion interaction and used the generalized gradient approximation (GGA) of Perdew–Burke–Ernzerhof (PBE) for the electron-electron exchange and correlation functional.[2,3] We corrected the van der Waals (VDW) forces using the D2 method proposed by Grimme.[4] After testing, we set the cutoff energy at 500 eV and employed a $2 \times 2 \times 1$ Monkhorst–Pack mesh for our calculations. We set the convergence criteria for the force at 0.02 eV Å^{-1} and for energy at 1×10^{-6} eV per atom. For the Fe 3d orbitals, we employed a correlation energy (U) of 3 eV and an exchange energy (J) of 0 eV (U-J = 3 eV).[5] We constructed a super-cell model using a carbon substrate that comprises 138 C atoms, 4 N atoms, and 1 Fe atom. After optimization, the slab's lattice parameters are a = b = 14.8 Å and c = 23.11 Å. An 18 Å vacuum layer was incorporated. Bader charge analysis was the basis for quantitative description of charge transfer.[6]

The Gibbs free energy (ΔG) can be represented by the following equation:

$$\Delta G=\Delta E+\Delta ZPE-T \cdot \Delta S \qquad (5)$$

Where ΔS is the reaction energy computed using DFT methods, ΔZPE denotes the changes in zero-point energies, and ΔS represents the entropy changes during the reaction.[7–9] In our study, the temperature (T) is set to 298.15 K.

The D-band center can be determined using the following formula:

$$\varepsilon_d = \frac{\int_{-\infty}^{\infty} n_d(\varepsilon)\varepsilon d\varepsilon}{\int_{-\infty}^{\infty} n_d(\varepsilon)d\varepsilon} \qquad (6)$$

The given equation represents the calculation formula for the D-band center. In this equation, ε represents the energy level, and $n_d(\varepsilon)$ corresponds to the density of states

(DOS) of the d orbitals in the material.
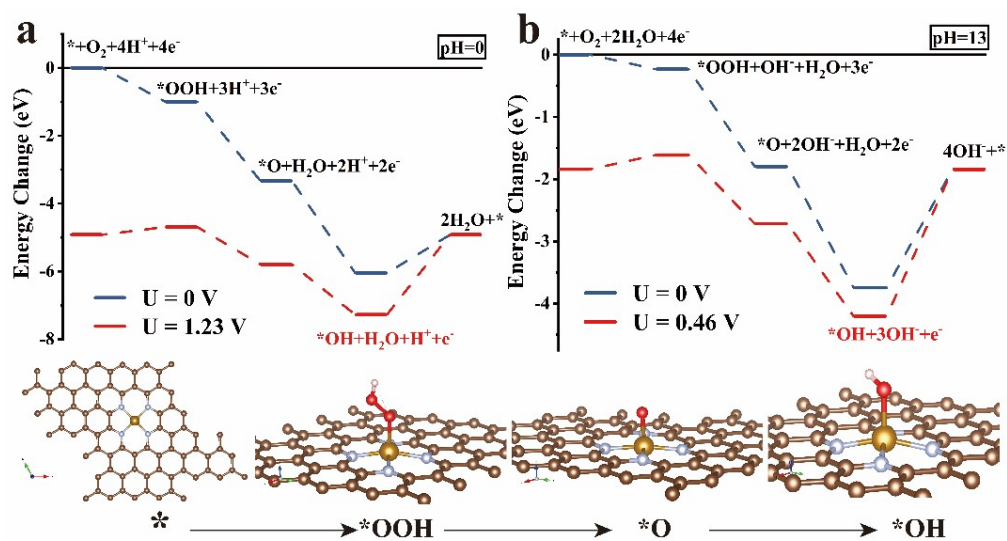
S3 Supplementary Figures and Tables

Fig. S1 The optimized structure of the ORR intermediates (*OOH, *O, *OH) on Fe-N_4 model and the free energy diagrams of Fe-N_4 with different pH corrections.
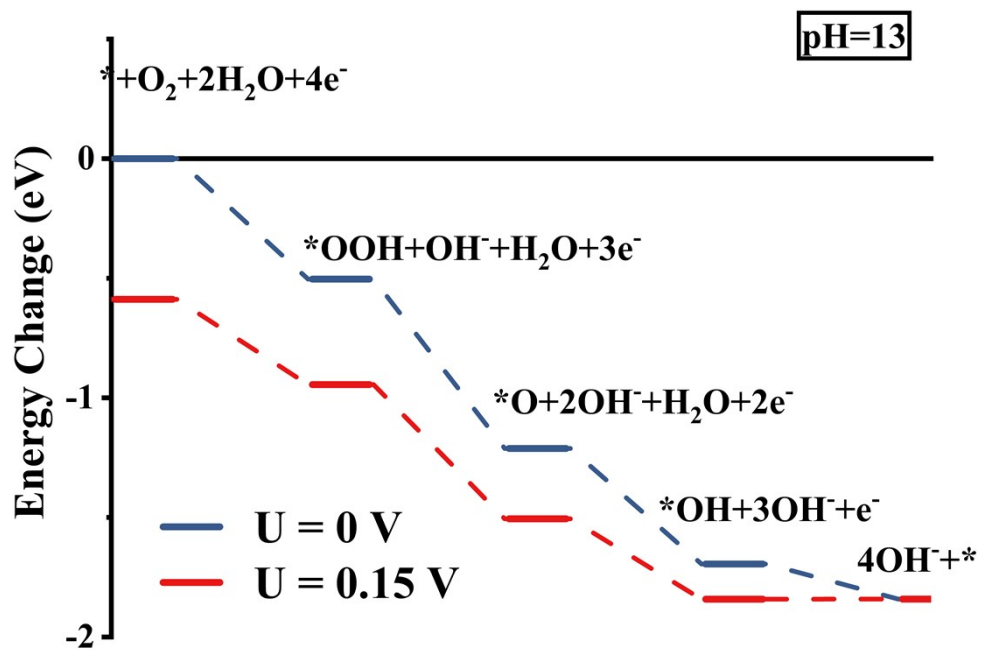
Fig. S2 The ORR free energy diagrams of Fe-N$_4$SP at different electrode potentials in alkaline electrolyte.
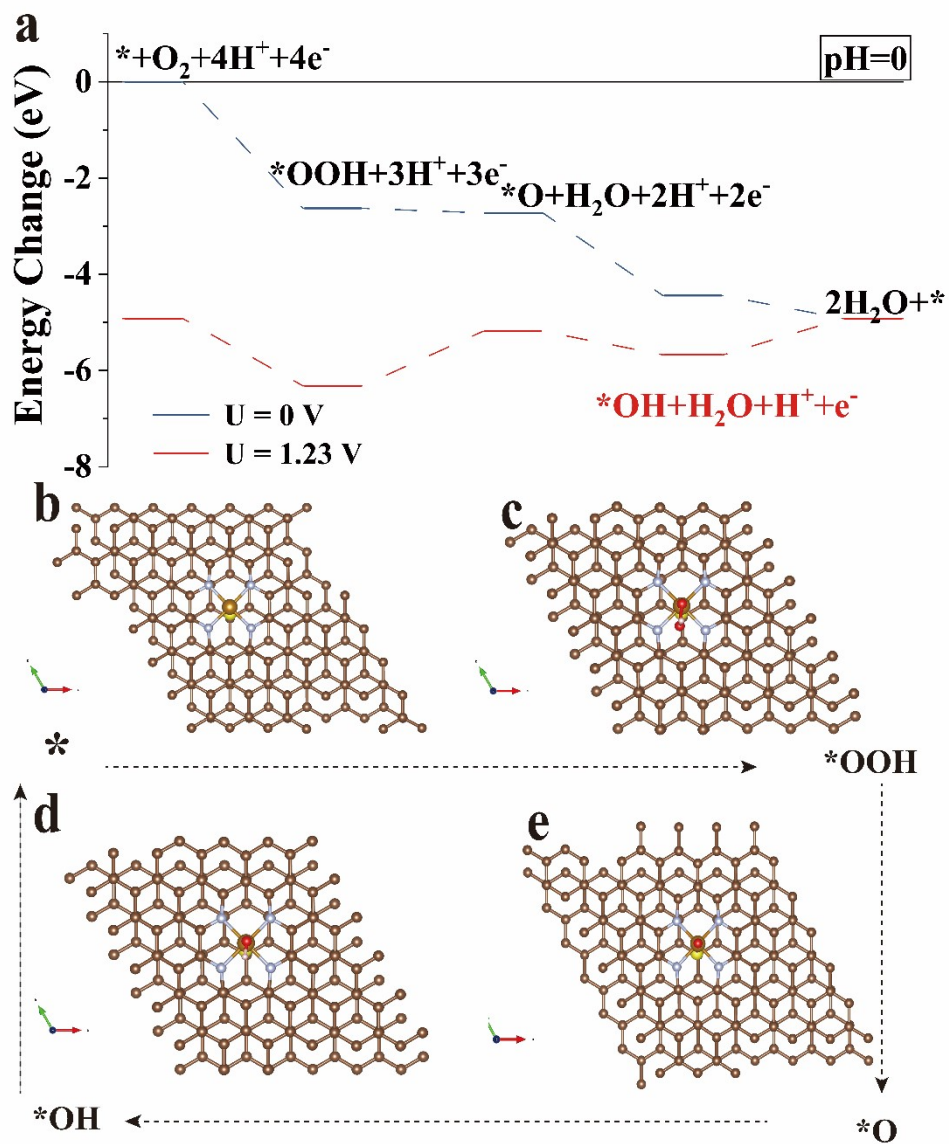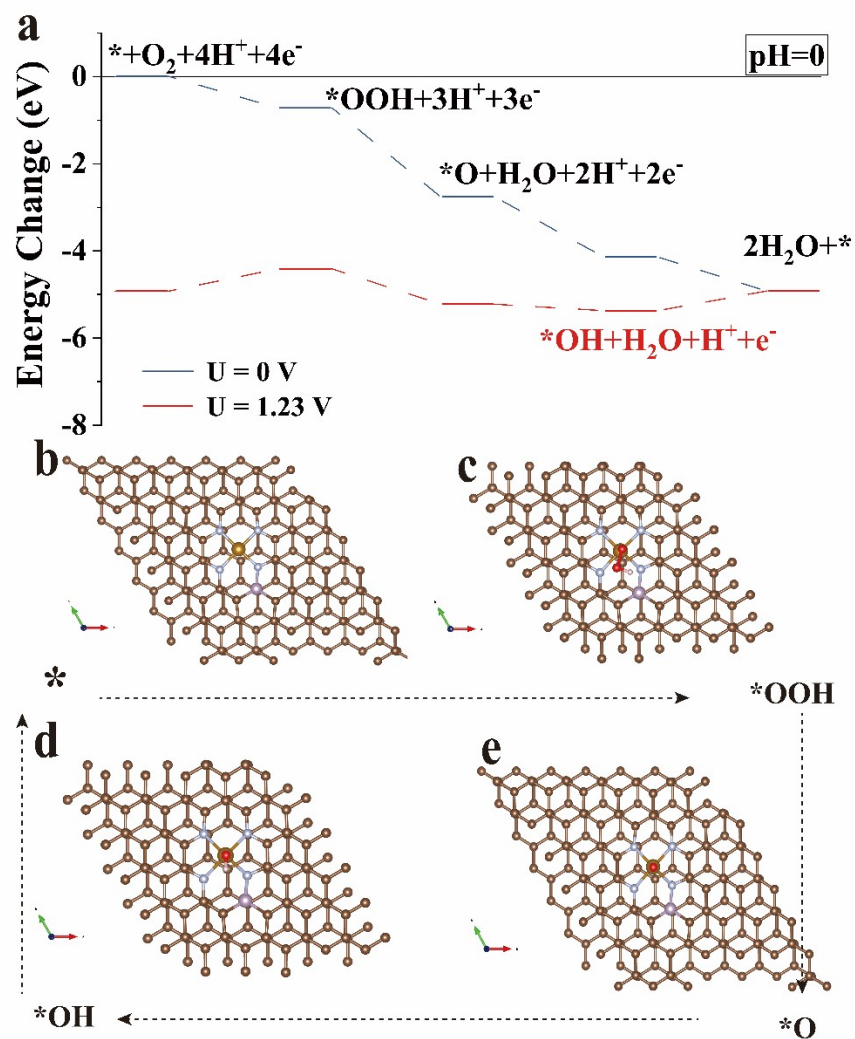
Fig. S3 The optimized structure of the ORR intermediates (*OOH, *O, *OH) on Fe-N$_4$S model and the free energy diagrams of Fe-N$_4$S model.

Fig. S4 The optimized structure of the ORR intermediates (*OOH, *O, *OH) on Fe-N$_4$P model and the free energy diagrams of Fe-N$_4$P model.
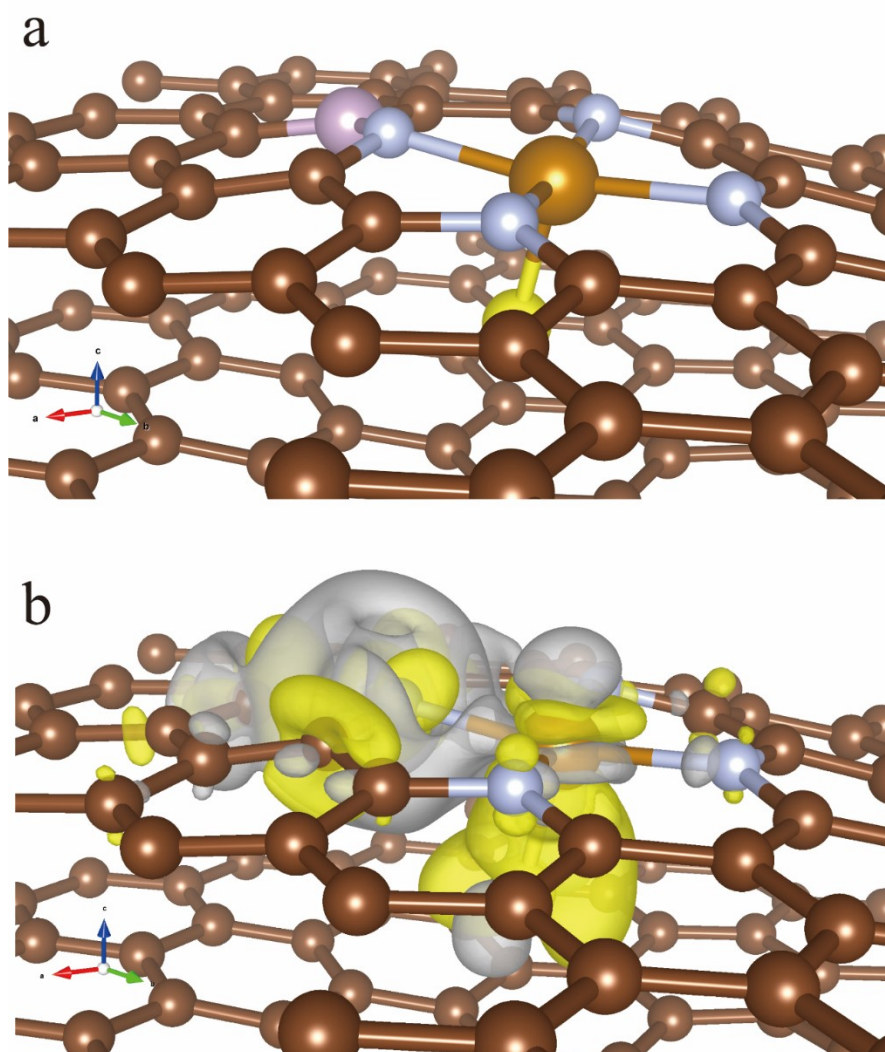
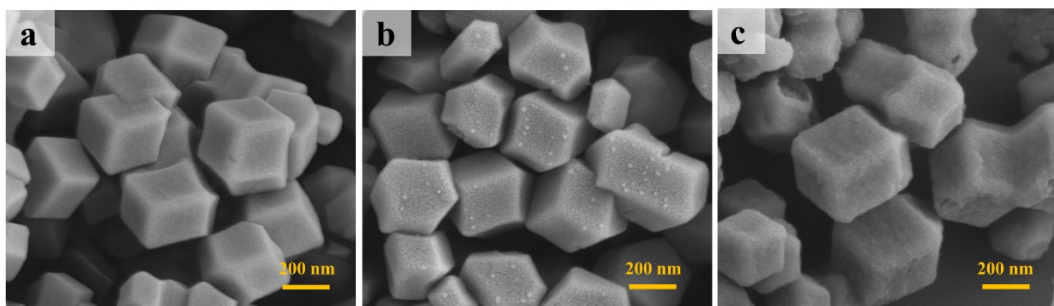Fig. S5 The optimized structure and differential charge density distribution of Fe-N$_4$SP model.

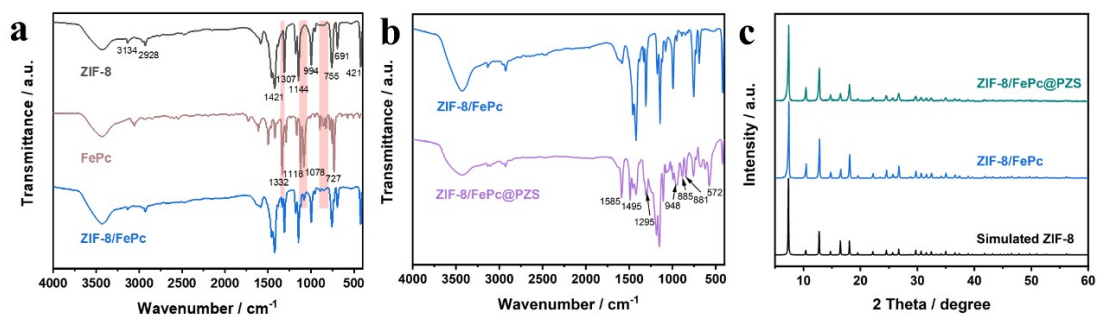Fig. S6 SEM images of (a) ZIF-8, (b) ZIF-8/FePc and (c) ZIF-8/FePc@PZS.

Fig. S7 (a, b) FT-IR patterns of the various samples, (c) XRD patterns of ZIF-8/FePc and ZIF-8/FePc@PZS.
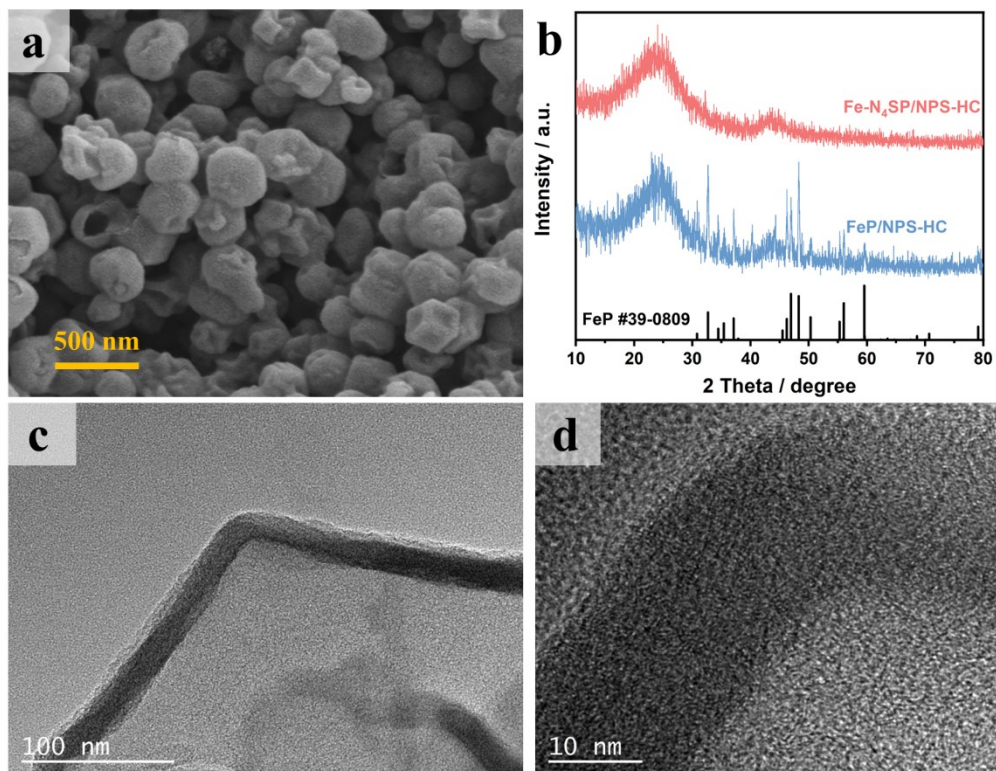
Fig. S8 (a) SEM image, (b) XRD patterns, (c) TEM and (d) HRTEM images of Fe-N$_4$SP/NPS-HC.
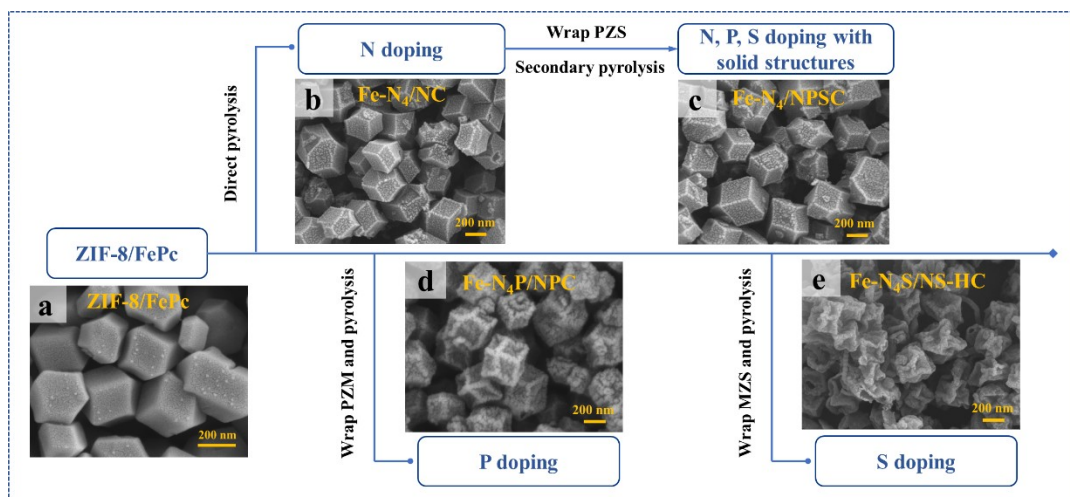
Fig. S9 SEM images of (a) ZIF-8/FePc, (b) Fe-N$_4$/NC, (c) Fe-N$_4$/NPSC, (d) Fe-N$_4$P/NPC and (e) Fe-N$_4$S/NS-HC.
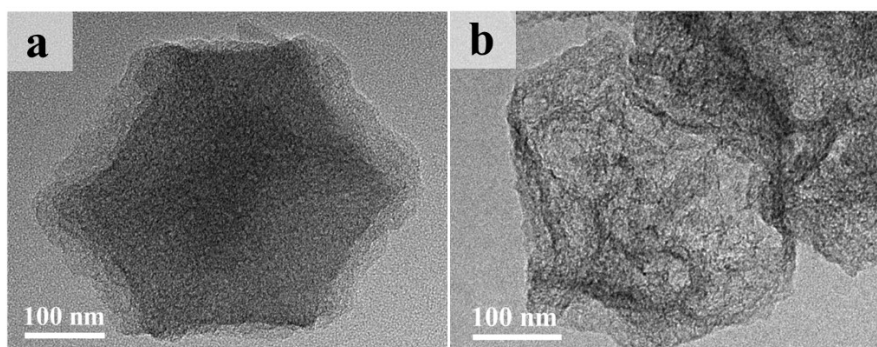

Fig. S10 TEM images of (a) Fe-N$_4$P/NPC and (b) Fe-N$_4$S/NS-HC.
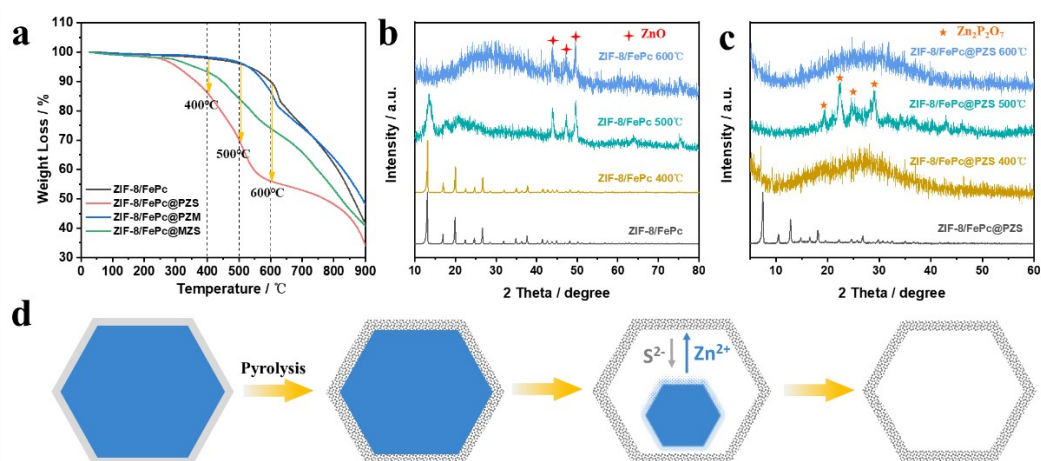

Fig. S11 (a) TG curve of ZIF-8 with different coating layers. XRD patterns of (b) ZIF-8/FePc and (c) ZIF-8/FePc@PZS with different pyrolysis temperatures. (d) Schematic diagram of the formation of hollow structure.
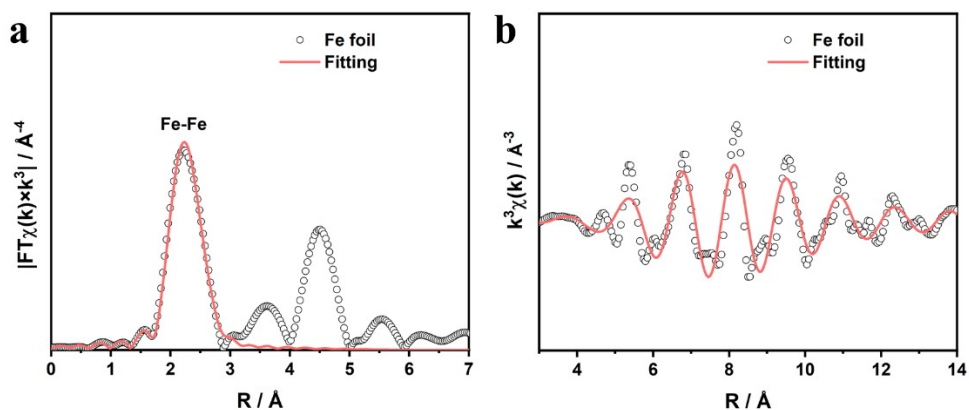
Fig. S12 The Fourier-transformed experimental EXAFS spectrum and fitted spectrum of Fe foil: (a) EXAFS R space, (b) EXAFS k space.
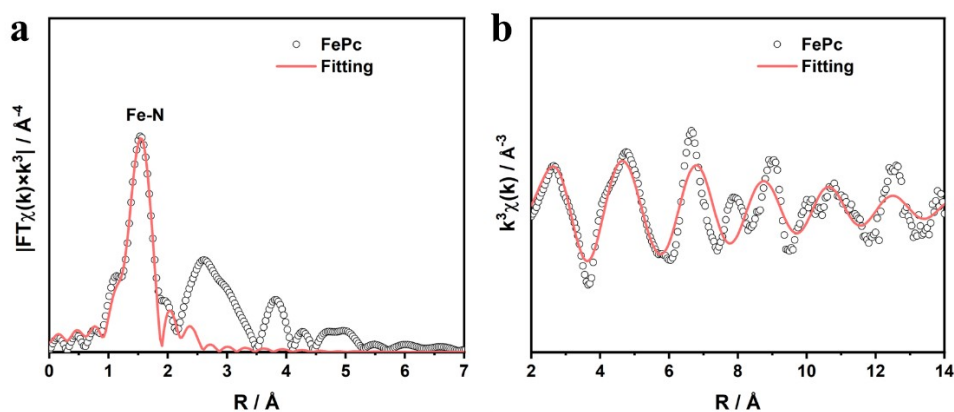

Fig. S13 The Fourier-transformed experimental EXAFS spectrum and fitted spectrum of FePc: (a) EXAFS R space, (b) EXAFS k space.
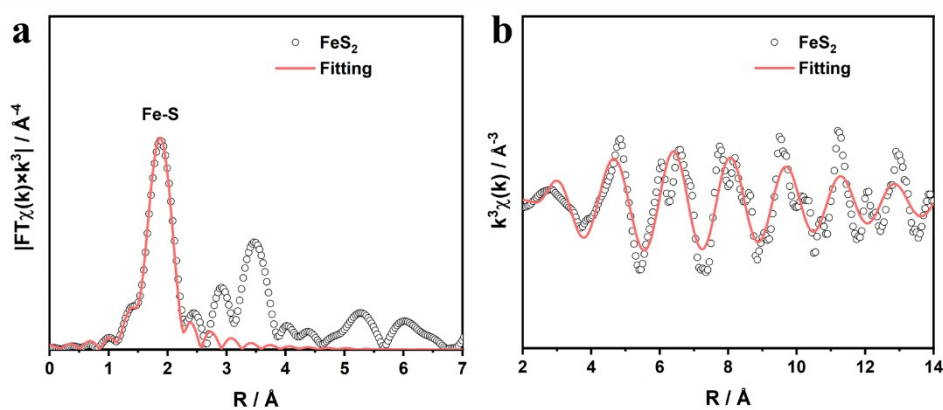
Fig. S14 The Fourier-transformed experimental EXAFS spectrum and fitted spectrum of FeS_2: (a) EXAFS R space, (b) EXAFS k space.
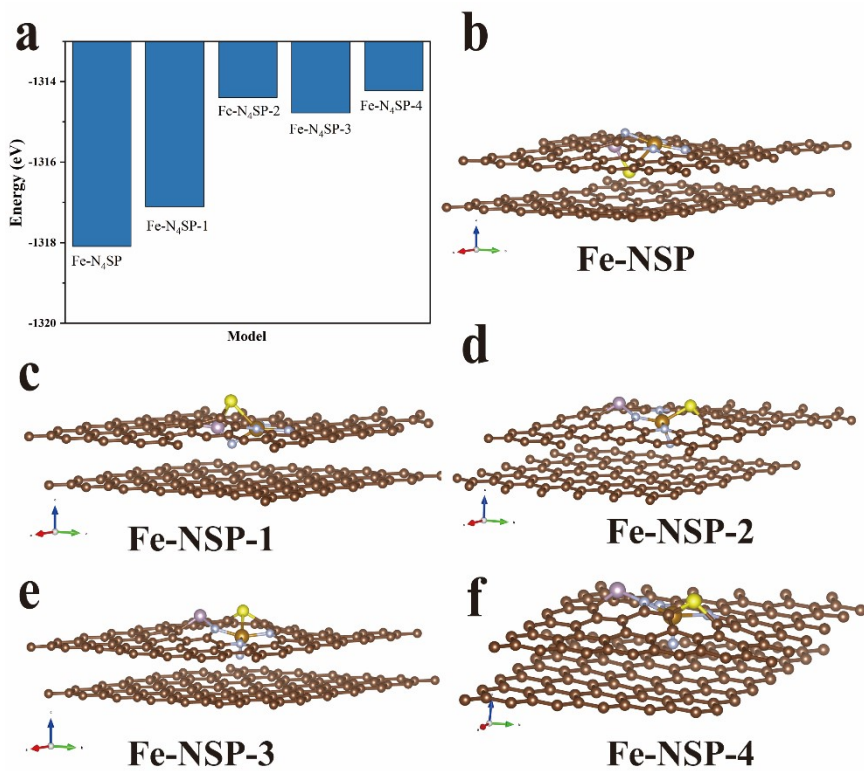
Fig. S15 All possible models with Fe-N and Fe-S coordination numbers of 4.0 and 1.1 and corresponding total energies.
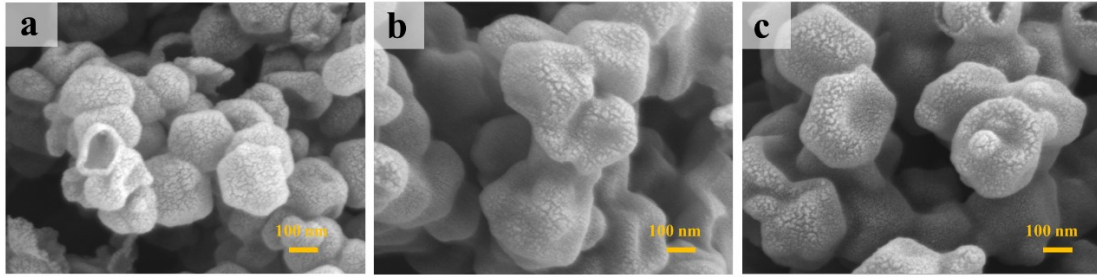
Fig. S16 SEM images of (a) Fe-N$_4$SP/NPS-HC-0.5, (b) Fe-N$_4$SP/NPS-HC-1.5 and (c) Fe-N$_4$SP/NPS-HC-2.
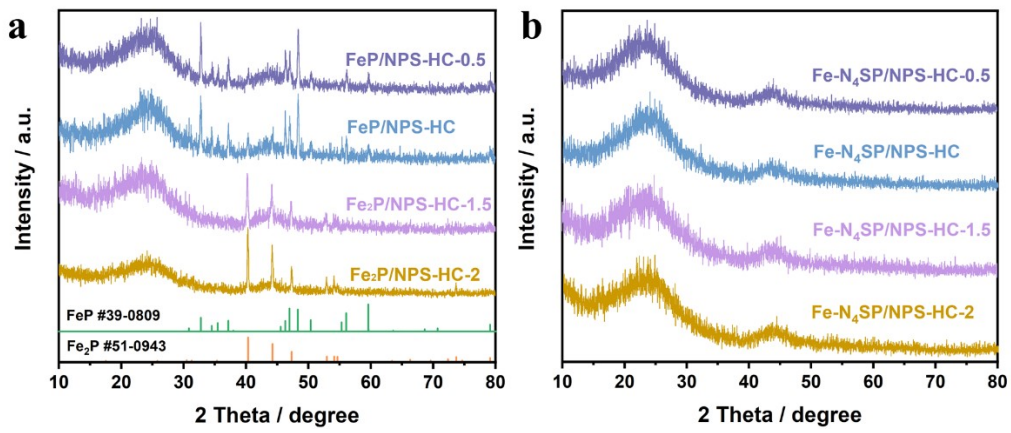
Fig. S17 XRD patterns of (a) after heat treatment and (b) after acid-etching of Fe-N$_4$SP/NPS-HC with different Fe content.
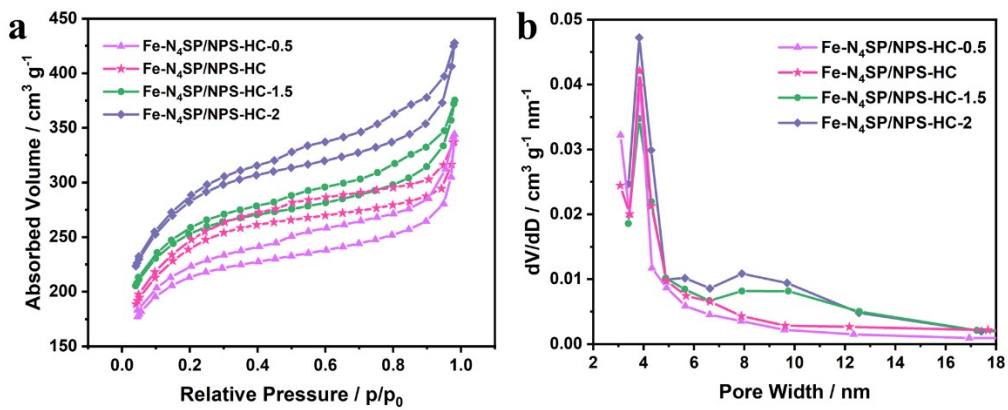
Fig.S18 (a) Nitrogen adsorption and desorption isotherms and (b) the pore size distribution of Fe-N$_4$SP/NPS-HC with different Fe content.
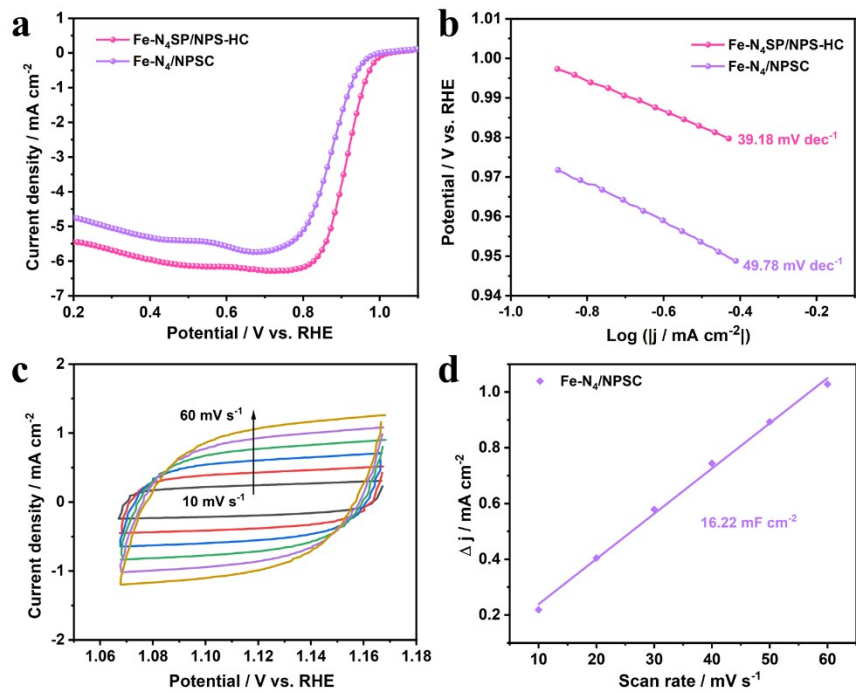
Fig. S19 LSV curves (a) and Tafel plots (b) of Fe-N$_4$SP/NPS-HC and Fe-N$_4$/NPSC. CV curves (c) and capacitive current (d) of Fe-N$_4$/NPSC at a series of scan rates (10~60 mV s^{-1}) in the ORR scanning range in 0.1 M KOH.
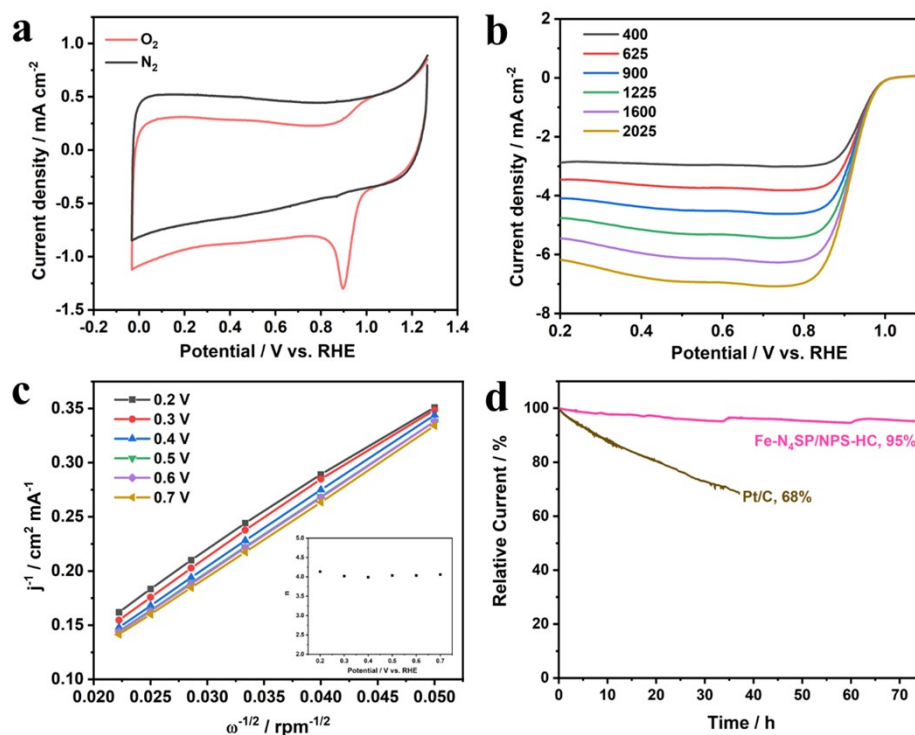
Fig. S20 (a) CV curves in N_2/O_2-saturated solutions, (b) LSV curves at different rotating rates, (c) K-L plots and the electron transfer number (inset) obtained from RDE tests of Fe-N_4SP/NPS-HC. (d) Current-time (i-t) chronoamperometric response of Fe-N_4SP/NPS-HC and Pt/C.

Note: the electron transfer number calculated from the K-L equation is slightly higher than 4, which may be due to the following reasons: 1) The thicker catalyst layer makes the K-L equation deviate from the ideal fluid dynamics model. The catalyst layer is usually thicker in the actual preparation to ensure a loading of 0.5 mg cm^{-2}. 2) The influence of the background current. The capacitance current of the carbon-based material is relatively large. 3) There is a deviation between the actual test conditions and the empirical constant values (e.g., O_2 concentration, O_2 diffusion coefficient, the kinetic viscosity of solution, and so on) involved in the K-L equation.
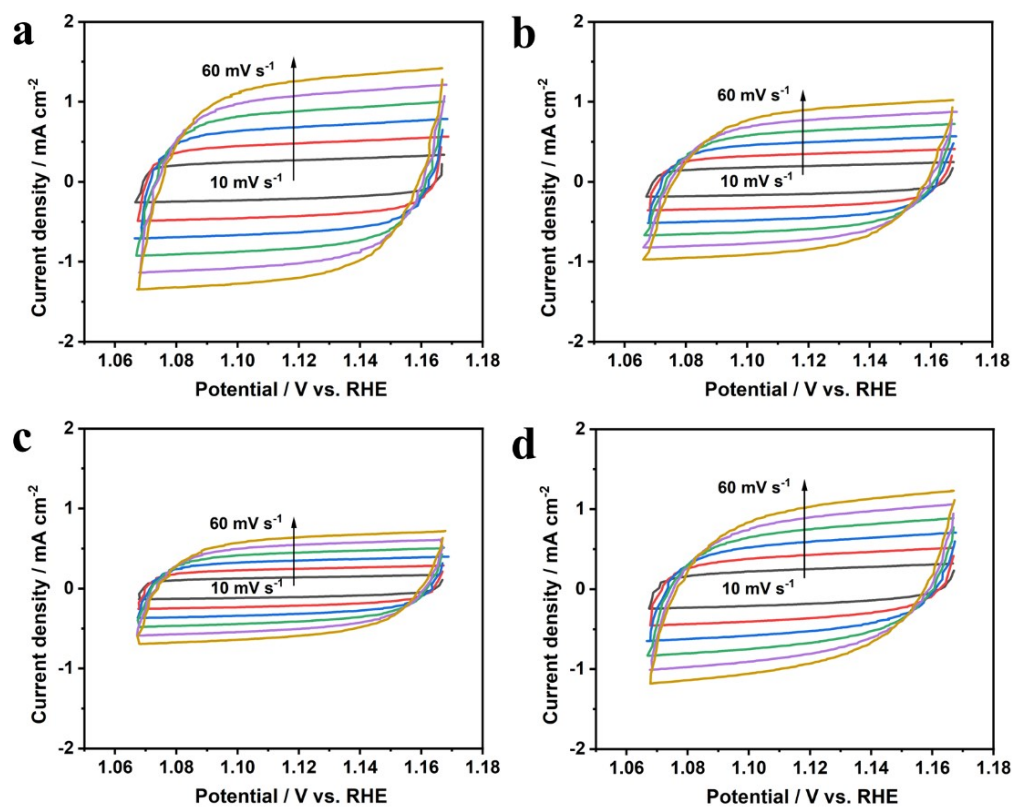
Fig. S21. CV plots of (a) Fe-N$_4$SP/NPS-HC, (b) Fe-N$_4$P/NPC, (c) Fe-N$_4$/NC, and (d) Pt/C at 10~60 mV s^{-1} in 0.1 M KOH.
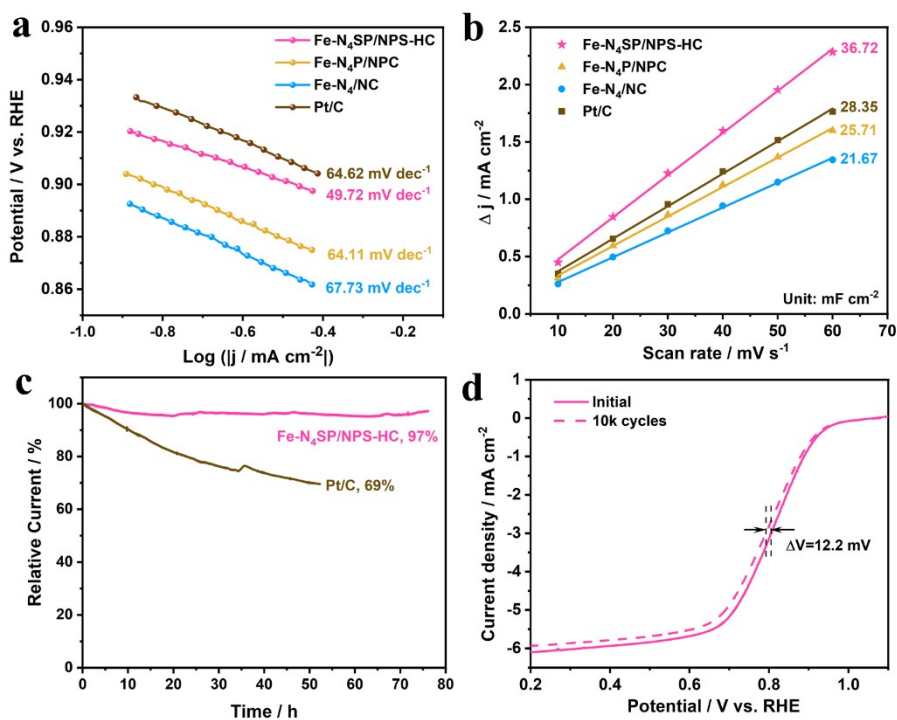
Fig. S22. (a) The Tafel plots and (b) electrochemical surface area evaluation of Fe-N$_4$SP/NPS-HC, Fe-N$_4$P/NPC, Fe-N$_4$/NC, and Pt/C in 0.1 M HClO$_4$. (c) Current time (i-t) chronoamperometric response of Fe-N$_4$SP/NPS-HC and Pt/C. (d) LSV before and after 10k CV cycles of Fe-N$_4$SP/NPS-HC.
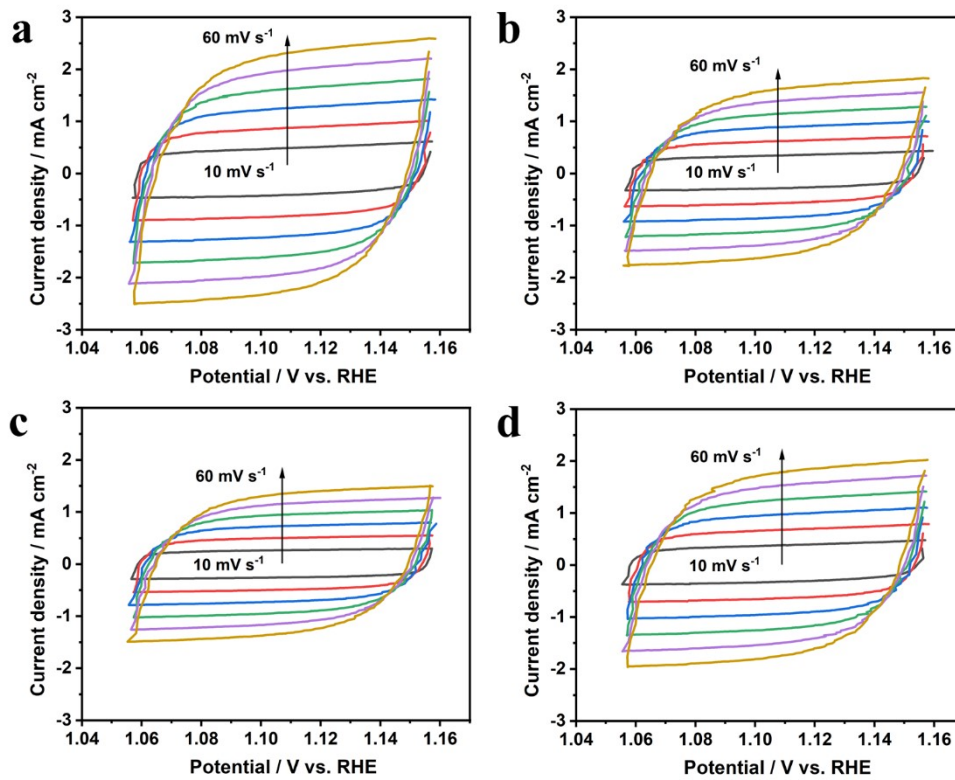
Fig. S23. CV plots of (a) Fe-N$_4$SP/NPS-HC, (b) Fe-N$_4$P/NPC, (c) Fe-N$_4$/NC, and (d) Pt/C at 10~60 mV s^{-1} in 0.1 M HClO$_4$.
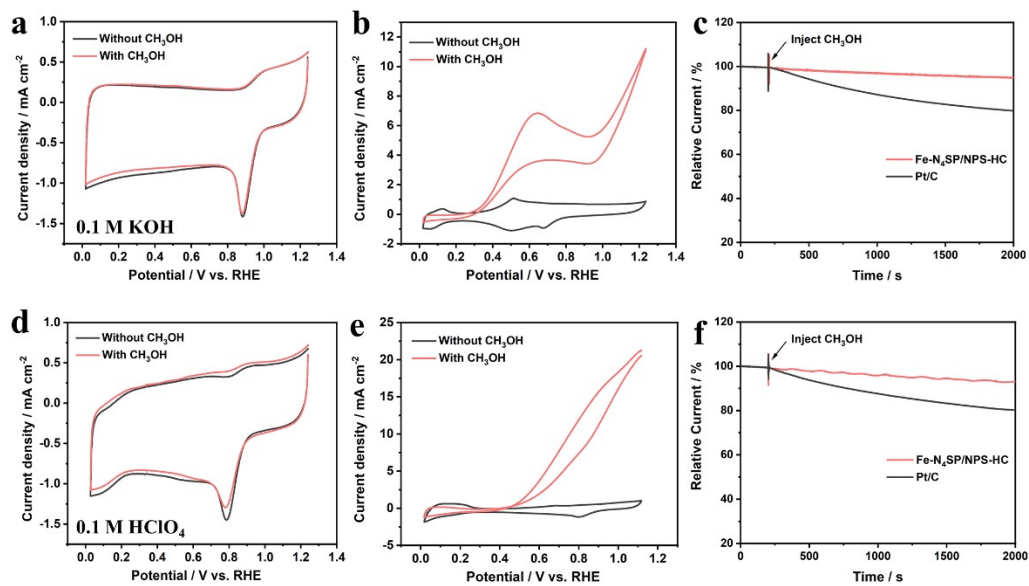
Fig. S24. CV curves for Fe-N$_4$SP/NPS-HC (a, d) and Pt/C (b, e), (c, f) chronoamperometric response for Fe-N$_4$SP/NPS-HC and Pt/C in O$_2$-saturated 0.1 M KOH/HClO$_4$ without and with 5 vol.% CH$_3$OH.
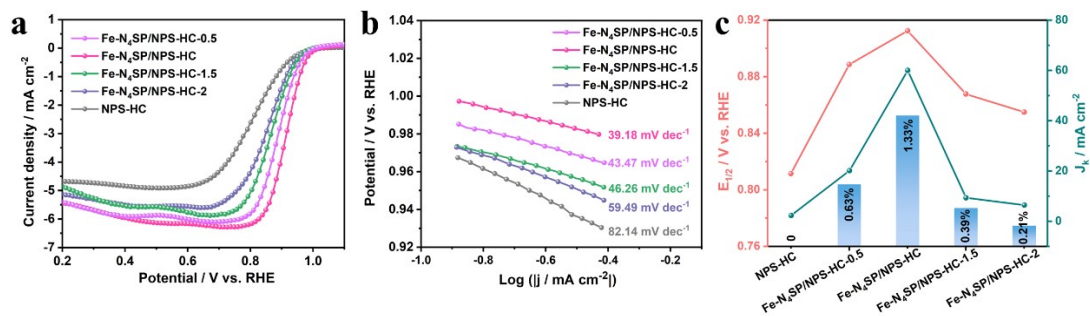
Fig. S25. The LSV curves (a) and Tafel plots (b) of Fe-N$_4$SP/NPS-HC with different Fe contents. (c) The variation curves of E$_{1/2}$ and J$_k$ with Fe content.
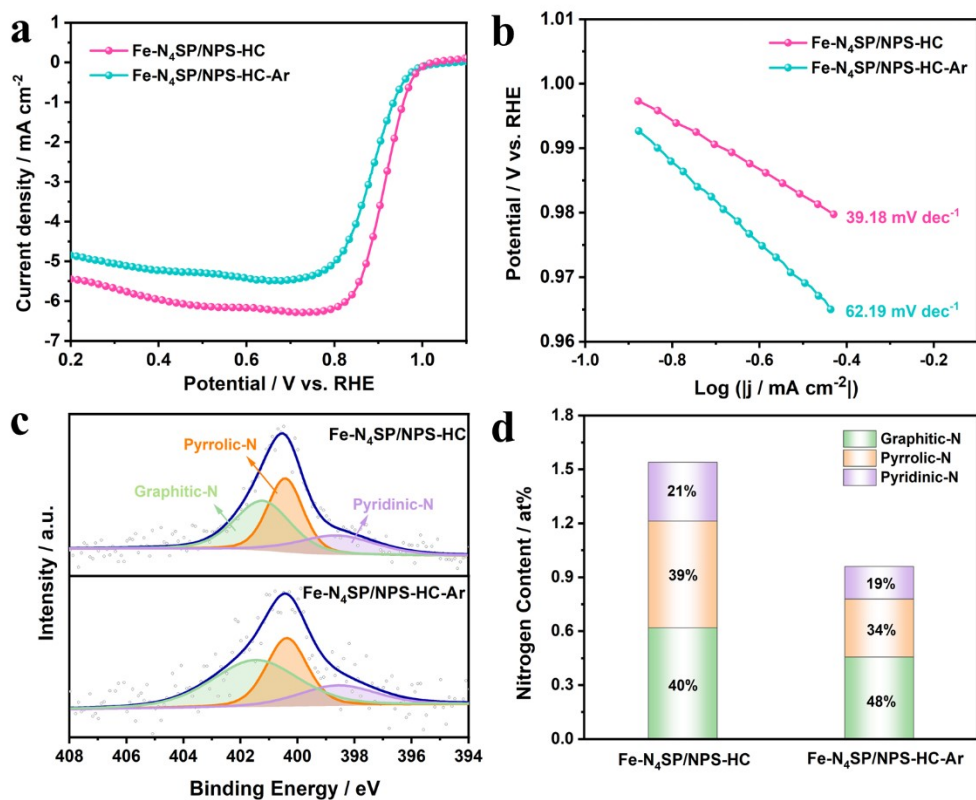
Fig. S26. (a) The LSV curves, (b) Tafel plots, (c) N1s XPS spectra and (d) comparison of pyrrolic-N and pyridinic-N contents of Fe-N$_4$SP/NPS-HC obtained in Ar/NH$_3$ and Ar atmosphere.

Fig. S27. (a) The open circuit voltage curves of Fe-N$_4$SP/NPS-HC (inset: photograph of the open-circuit potential). (b) Galvanostatic discharge curves at a current density of 5 mA cm^{-2}.

Fig. S28. The performance comparison of rechargeable Zn-air batteries of the recently reported single-atom catalysts.
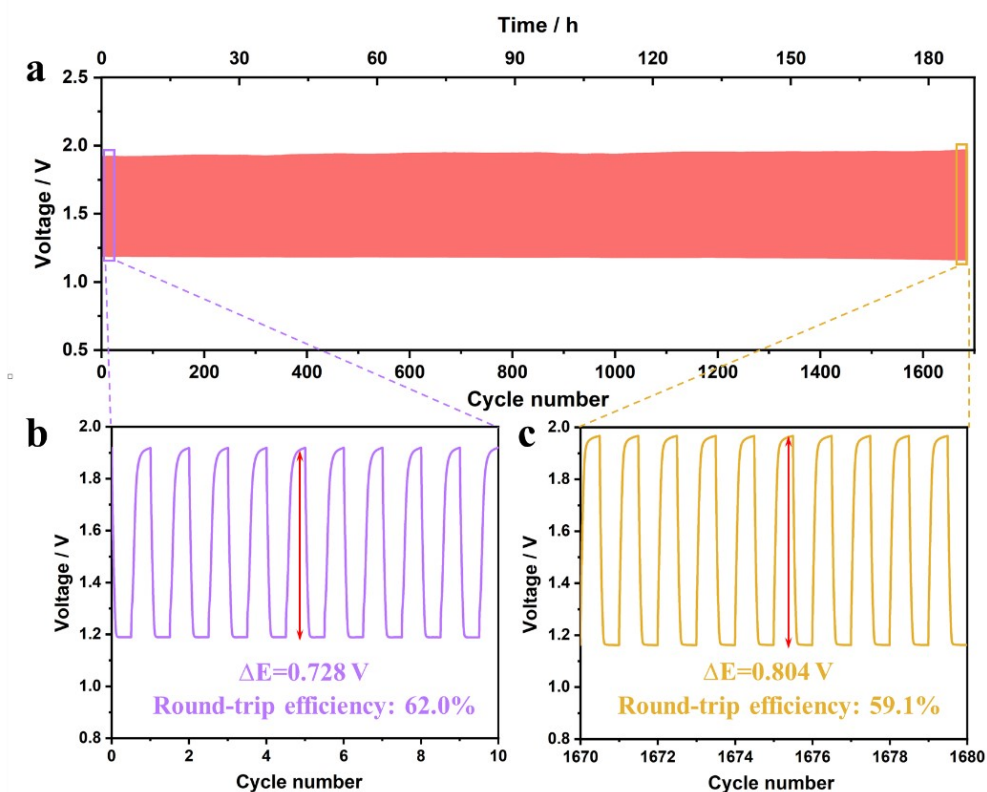
Fig. S29 (a) Charge/discharge cycling stabilities of Fe-N$_4$SP/NPS-HC at a current density of 5 mA cm^{-2} without updating electrolyte. (b, c) Charge/discharge cycle curves and round-trip efficiency for different cycles.

The charge/discharge cycling stabilities of Fe-N$_4$SP/NPS-HC-based ZAB were also measured without updating electrolyte. Significantly, ZAB based on Fe-N4SP/NPS-HC also exhibited excellent cycling stability, with the voltage gap increasing by only 76 mV ($\approx$10% relative to the initial) and a high round-trip efficiency of 59% after continuous operation for over 188 h. This result confirms that the prepared Fe-N$_4$SP/NPS-HC catalysts with highly coordinated structures have good potential for practical applications.
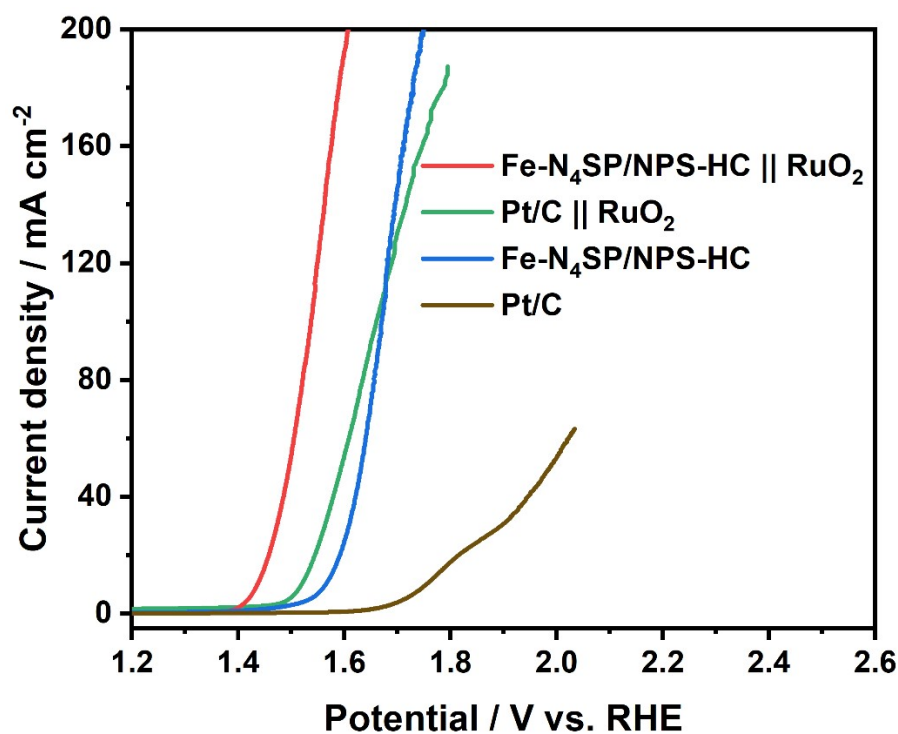
Fig. S30 OER LSV curves with iR corrected of different catalysts.

The charging process of zinc-air batteries is closely associated to oxygen evolution reaction (OER), so in order to investigate the reason for the decrease of charging voltage during the cycling process, we tested the OER performance of different catalysts. As shown in Fig. S30, Fe-N_4SP/NPS-HC showed a better OER activity with overpotential of 334 mV at 10 mA cm^{-2}, far below that of Pt/C (525 mV). After mixing with RuO_2, the OER activities were significantly increased. The overpotential of Fe-N_4SP/NPS-HC ‖ RuO_2 was reduced to 207 mV, also lower than that of Pt/C ‖ RuO_2 (291 mV). Therefore, the as-prepared Fe-N_4SP/NPS-HC catalysts also contributed part of the OER activity in mixed cathode catalysts, and enhanced OER performance resulted in a lower charging voltage of ZAB based on Fe-N_4SP/NPS-HC‖ RuO_2 than that of based on Pt/C ‖ RuO_2. The lower charging voltage reduces the side reaction of air cathode during the charging process, greatly extending the cycle life of rechargeable ZABs.

Table S1 The element content in Fe-N$_4$SP/NPS-HC determined by ICP and XPS.

Element	C	Fe	N	P	S
ICP-OES	-	1.33%	-	3.90%	2.15%
XPS (At.%)	91.79%	0.36%	5.85%	1.28%	0.72%

Table S2. EXAFS fitting parameters at the Fe K-edge for various samples

Sample	Shell	CN^a	$R(Å)^b$	$\sigma^2(Å^2)^c$	$\Delta E_0(eV)^d$	R factor
Fe foil	Fe-Fe1	8*	2.49±0.01	0.0056	9.7	0.0056
	Fe-Fe2	6*	2.86±0.01	0.0089	9.1	
FePc	Fe-N	4.0±0.4	1.96±0.01	0.0049	9.9	0.0154
FeS$_2$	Fe-S	5.7±0.3	2.26±0.01	0.0045	9.2	0.0193
Fe-N$_4$SP /NPS-HC	Fe-N	4.0±0.4	1.96±0.01	0.0059	8.1	0.0148
	Fe-S	1.1±0.2	2.24±0.01	0.0056	2.4	

[a]CN, coordination number; [b]R, distance between absorber and backscatter atoms; [c]σ^2, Debye-Waller factor to account for both thermal and structural disorders; [d]ΔE_0, inner potential correction; R factor indicates the goodness of the fit. S_0^2 was fixed to 0.86, according to the experimental EXAFS fit of Fe foil by fixing CN as the known crystallographic value. A reasonable range of EXAFS fitting parameters: $0.600 < S_0^2 < 1.000$; $CN > 0$; $\sigma^2 > 0$ Å^2; $|\Delta E_0| < 15$ eV; R factor < 0.02.

Table S3 Fe content of different samples determined by ICP.

Samples	Fe-N$_4$SP /NPS-HC-0.5	Fe-N$_4$SP /NPS-HC	Fe-N$_4$SP /NPS-HC-1.5	Fe-N$_4$SP /NPS-HC-2
ICP	0.63%	1.33%	0.39%	0.21%

Table S4 BET surface area of Fe-N$_4$SP/NPS-HC with different Fe content.

Samples	Fe-N$_4$SP /NPS-HC-0.5	Fe-N$_4$SP /NPS-HC	Fe-N$_4$SP /NPS-HC-1.5	Fe-N$_4$SP /NPS-HC-2
BET Surface Area (m^2/g)	793.945	865.938	934.918	1023.608

Table S5. Comparison of the ORR activity of the recently reported single-atom catalysts in 0.1 M KOH.

Catalysts	$E_{1/2}$ / V	J_K / mA cm^{-2}	Tafel / mV dec^{-1}	References
Fe-N$_4$SP/NPS-HC	0.912	60 (at 0.85 V)	39.18	This work
FeN$_4$-700/900	0.904	28.4 (at 0.8 V)	71	10
Fe$_3$Co$_7$-NC	0.893	6.08	56	11
Fe-NHC	0.89	-	53.7	12
Fe/SNCFs-NH$_3$	0.89	38.36 (at 0.82 V)	70.82	13
Fe/Fe$_x$C@Fe-N-C-900	0.91	19.84 (at 0.85 V)	44.8	14
FeCo-N-HCN	0.86	-	52.1	15
FeN$_3$OS	0.874	17 (at 0.85 V)	55	16
Fe/N-CNRs	0.9	22.04 (at 0.85 V)	69.05	17
Fe-OAC	0.854	-	58	18
Fe@Fe-N-C	0.916	60.9	66.3	19
Fe-N-C	0.905	23.9	64.3	
Fe-NC SACc	0.85	-	48	20
Fe SA/NPCs	0.83	35.42 (at 0.85 V)	65.3	21
Fe$_1$-HNC	0.842	-	51.5	22
Fe-SAC/NC	0.84	-	46	23
Fe-N/P-C-700	0.867	24.49	-	24
Fe/N-G-SAC	0.89	3.837 (at 0.9 V)	50	25
Fe/NC-3	0.9	-	100.7	26
FeNSC-2Fe	0.913	15.7 (at 0.85 V)	59	27
P-doped Fe-N-C	0.882	30.5 (at 0.82 V)	82	28
FeMo$_2$/NC	0.91	82.28 (at 0.85 V)	54	29
Fe/Zn-N-C	0.906	-	74	30

Table S6. Comparison of the ORR activity of the recently reported single-atom catalysts in acid electrolyte.

Catalysts	$E_{1/2}$ / V	J_K / mA cm^{-2}	Tafel / mV dec^{-1}	Electrolyte	References
Fe-N$_4$SP/NPS-HC	0.814	46.7 (at 0.7 V)	49.72	0.1 M HClO$_4$	This work
Fe/Fe$_x$C@Fe-N-C-900	0.81	95.8 (at 0.75 V)	81.9	0.1 M HClO$_4$	14
FeCo-N-HCN	0.75	-	86.5	0.5 M H$_2$SO$_4$	15
Fe-OAC	0.71	6.57 (at 0.7 V)	61	0.1 M HClO$_4$	18
Fe@Fe-N-C	0.829	11.1 (at 0.8 V)	75.5	0.1 M HClO$_4$	19
Fe-N-C	0.807	5.07 (at 0.8 V)	76.3	0.1 M HClO$_4$	19
Fe SA/NPCs	0.77	5.8 (at 0.85 V)	70.7	0.5 M H$_2$SO$_4$	21
Fe-SAC/NC	0.69	-	45	0.5 M H$_2$SO$_4$	23
FeMo$_2$/NC	0.8	38 (at 0.75 V)	57	0.5 M H$_2$SO$_4$	29
Fe/Zn-N-C	0.808	-	79	0.1 M HClO$_4$	30
Fe@MNC-OAc	0.838	15.87 (at 0.8 V)	70.4	0.1 M HClO$_4$	31
Fe-N$_4$/C-60	0.8	37 (at 0.75 V)	68	0.1 M HClO$_4$	32
Fe$_{SA}$/Fe$_{AC}$-2DNPC	0.81	-	54.5	0.5 M H$_2$SO$_4$	33
Fe-N-C/FeN	0.81	11.24 (at 0.8 V)	80	0.1 M HClO$_4$	34
Fe$_{SA}$/NMC-800	0.71	41 (at 0.6 V)	68	0.1 M HClO$_4$	35

Table S7. The performance comparison of rechargeable Zn-air batteries.

Catalysts	Peak power density / mW cm^{-2}	Specific capacity / mAh g$_{Zn}^{-1}$	Stability	References
Fe-N$_4$SP/NPS-HC	225	893	5 mA cm^{-2} for 320 h	This work
FeN$_4$-700/900	164.4	695	2 mA cm^{-2} for 96 h	10
Fe-NHC	157	755.8	10 mA cm^{-2} for 64 h	12
Fe/SNCFs-NH$_3$	255.84	-	5 mA cm^{-2} for 300 h	13
Fe/Fe$_x$C@Fe-N-C-900	150	818	10 mA cm^{-2} for 65 h	14
Fe/N-CNRs	181.8	771.8	10 mA cm^{-2} for 100 h	17
Fe-OAC	113	710	-	18
Fe@Fe-N-C	228.7	806.7	-	19
Fe-N/P-C-700	133.2	723.6	10 mA cm^{-2} for 40 h	24
P-doped Fe-N-C	201	-	1 mA cm^{-2} for 600 h	28
S-modified Fe-N-C	117.2	766.5	10 mA cm^{-2} for 100 h	36
Fe-OES	186.8	807.5	5 mA cm^{-2} for 130 h	37
FeN$_4$Cl$_1$/NC	170	801	10 mA cm^{-2} for 100 h	38

S4. References

1   G. G. Kresse and J. J. Furthmüller, *Phys. Rev. B*, 1996, **54**, 11169–11186.

2   J. P. Perdew, K. Burke and M. Ernzerhof, *Phys. Rev. Lett.*, 1996, **77**, 3865–3868.

3   B. Hammer, L. B. Hansen and J. K. Nørskov, *Phys. Rev. B*, 1999, **59**, 7413–7421.

4   S. Grimme, *J. Comput. Chem.*, 2006, **27**, 1787–1799.

5   K. Liu, J. Fu, Y. Lin, T. Luo, G. Ni, H. Li, Z. Lin and M. Liu, *Nat. Commun.*, 2022, **13**, 2075.

6   W. Tang, E. Sanville and G. Henkelman, *J. Phys.: Condens. Matter*, 2009, **21**, 084204.

7   J. K. Nørskov, J. Rossmeisl, A. Logadottir, L. Lindqvist, J. R. Kitchin, T. Bligaard and H. Jónsson, *J. Phys. Chem. B*, 2004, **108**, 17886–17892.

8   J. K. Nørskov, T. Bligaard, A. Logadottir, J. R. Kitchin, J. G. Chen, S. Pandelov and U. Stimming, *J. Electrochem. Soc.*, 2005, **152**, J23.

9   A. A. Peterson, F. Abild-Pedersen, F. Studt, J. Rossmeisl and J. K. Nørskov, *Energy Environ. Sci.*, 2010, **3**, 1311–1315.

10   B. Zhao, D. Xue, P. Yuan, W. Yan, J. Zhang, S. Mu and J.-N. Zhang, *Appl. Catal. B: Environ.*, 2023, **324**, 122251.

11   T. Gu, D. Zhang, Y. Yang, C. Peng, D. Xue, C. Zhi, M. Zhu and J. Liu, *Adv. Funct. Mater.*, 2023, **33**, 2212299.

12   S. Zhang, W. Yang, Y. Liang, X. Yang, M. Cao and R. Cao, *Appl. Catal. B: Environ.*, 2021, **285**, 119780.

13   L. Yang, X. Zhang, L. Yu, J. Hou, Z. Zhou and R. Lv, *Adv. Mater.*, 2022, **34**, 2105410.

14   M. Chen, F. Kong, H. Yao, Y. Chen, G. Meng, Z. Chang, C. Chen, H. Tian, L. Wang, X. Cui and J. Shi, *Chem. Eng. J.*, 2023, **453**, 139820.

15   H. Li, Y. Wen, M. Jiang, Y. Yao, H. Zhou, Z. Huang, J. Li, S. Jiao, Y. Kuang and S. Luo, *Adv. Funct. Mater.*, 2021, **31**, 2011289.

16   L. Yu, Y. Li and Y. Ruan, *Angew. Chem. Int. Ed.*, 2021, **60**, 25296–25301.

17   X. Gong, J. Zhu, J. Li, R. Gao, Q. Zhou, Z. Zhang, H. Dou, L. Zhao, X. Sui, J. Cai, Y. Zhang, B. Liu, Y. Hu, A. Yu, S. Sun, Z. Wang and Z. Chen, *Adv. Funct. Mater.*, 2021, **31**, 2008085.

18   L. Deng, L. Qiu, R. Hu, L. Yao, Z. Zheng, X. Ren, Y. Li and C. He, *Appl. Catal. B: Environ.*, 2022, **305**, 121058.

19   L. Li, Y. Wen, G. Han, F. Kong, L. Du, Y. Ma, P. Zuo, C. Du and G. Yin, *Small*, 2023, 2300758.

20   L. Zhao, Y. Zhang, L.-B. Huang, X.-Z. Liu, Q.-H. Zhang, C. He, Z.-Y. Wu, L.-J. Zhang, J. Wu, W. Yang, L. Gu, J.-S. Hu and L.-J. Wan, *Nat. Commun.*, 2019, **10**, 1278.

21   H. Yang, Z. Li, S. Kou, G. Lu and Z. Liu, *Appl. Catal. B: Environ.*, 2020, **278**, 119270.

22   X. Zhang, S. Zhang, Y. Yang, L. Wang, Z. Mu, H. Zhu, X. Zhu, H. Xing, H. Xia, B. Huang, J. Li, S. Guo and E. Wang, *Adv. Mater.*, 2020, **32**, 1906905.

23   J. Hu, D. Wu, C. Zhu, C. Hao, C. Xin, J. Zhang, J. Guo, N. Li, G. Zhang and Y. Shi, *Nano Energy*, 2020, **72**, 104670.

24   K. Yuan, D. Lützenkirchen-Hecht, L. Li, L. Shuai, Y. Li, R. Cao, M. Qiu, X. Zhuang, M. K. H. Leung, Y. Chen and U. Scherf, *J. Am. Chem. Soc.*, 2020, **142**, 2404–2412.

25   M. Xiao, Z. Xing, Z. Jin, C. Liu, J. Ge, J. Zhu, Y. Wang, X. Zhao and Z. Chen, *Adv. Mater.*, 2020, **32**, 2004900.

26   M. Liu, J. Lee, T.-C. Yang, F. Zheng, J. Zhao, C.-M. Yang and L. Y. S. Lee, *Small Methods*, 2021, **5**, 2001165.

27 C. Shao, L. Wu, Y. Wang, K. Qu, H. Chu, L. Sun, J. Ye, B. Li and X. Wang, *Appl. Catal. B: Environ.*, 2022, **316**, 121607.

28 J. Sheng, S. Sun, G. Jia, S. Zhu and Y. Li, *ACS Nano*, 2022, **16**, 15994–16002.

29 J. Hu, C. Zhang, M. Sun, Q. Qi, S. Luo, H. Song, J. Xiao, B. Huang, M. K. H. Leung and Y. Zhang, *Nano Res.*, 2022, **15**, 4950–4957.

30 H. Li, S. Di, P. Niu, S. Wang, J. Wang and L. Li, *Energy Environ. Sci.*, 2022, **15**, 1601–1610.

31 Y. Liu, F. Tu, Z. Zhang, Z. Zhao, P. Guo, L. Shen, Y. Zhang, L. Zhao, G. Shao and Z. Wang, *Appl. Catal. B: Environ.*, 2023, **324**, 122209.

32 X. Wang, Y. Jia, X. Mao, D. Liu, W. He, J. Li, J. Liu, X. Yan, J. Chen, L. Song, A. Du and X. Yao, *Adv. Mater.*, 2020, **32**, 2000966.

33 X. Wan, Q. Liu, J. Liu, S. Liu, X. Liu, L. Zheng, J. Shang, R. Yu and J. Shui, *Nat. Commun.*, 2022, **13**, 2963.

34 X. Luo, X. Wei, H. Wang, W. Gu, T. Kaneko, Y. Yoshida, X. Zhao and C. Zhu, *Nano-Micro Lett.*, 2020, **12**, 163.

35 H. Xie, B. Du, X. Huang, D. Zeng, H. Meng, H. Lin, W. Li, T. Asefa and Y. Meng, *Small*, 2023, 2303214.

36 S. Li, L. Xia, J. Li, Z. Chen, W. Zhang, J. Zhu, R. Yu, F. Liu, S. Lee, Y. Zhao, L. Zhou and L. Mai, *Energy Environ. Mater.*, 2022, e12560.

37 C. Hou, L. Zou, L. Sun, K. Zhang, Z. Liu, Y. Li, C. Li, R. Zou, J. Yu and Q. Xu, *Angew. Chem. Int. Ed.*, 2020, **132**, 7454–7459.

38 L. Hu, C. Dai, L. Chen, Y. Zhu, Y. Hao, Q. Zhang, L. Gu, X. Feng, S. Yuan, L. Wang and B. Wang, *Angew. Chem. Int. Ed.*, 2021, **60**, 27324–27329.